Effect of Heat Treatment on Microstructure and Mechanical Behaviours of 18Ni-300 Maraging Steel Manufactured by Selective Laser Melting

Jun Song [a], Qian Tang [a,*], Qixiang Feng [a], Shuai Ma [a], Rossitza Setchi [b], Ying Liu [b], Quanquan Han [b], Xiaojie Fan [a], Mengxiang Zhang [c]

a State Key Laboratory of Mechanical Transmission, Chongqing University, Chongqing 400044, China

b Cardiff School of Engineering, Cardiff University, Cardiff CF24 3AA, UK

c Chongqing Shining Technology Co., Ltd., Chongqing 401120, China

Abstract

Selective laser melting (SLM) of 18Ni-300 maraging steel is an important research area in view of its numerous applications in the automotive domain. Heat treatment plays a significant role in the microstructure and mechanical behaviour of maraging steels and is a major area of interest. This paper investigated the effect of heat treatment on microstructure and mechanical behaviour of SLM-built 18Ni-300 maraging steel. The experimental results showed that the densest parts with the smallest number of defects were fabricated at optimum laser energy density of 70 J/mm^3 and laser power of 275 W. When the laser power was fixed at 275 W, lower laser energy density resulted in the formation of balling and irregular pores, while higher laser energy density induced spherical pores and microcracks. The as-built samples consisted of cellular and columnar microstructures due to the fast cooling and solidification rates during SLM. However, solution treatment led to changes in the typical microstructure and massive lath martensite phase. The tensile strength and microhardness decreased slightly due to grain growth and residual stress relief upon solution treatment; an opposite effect was observed when the samples were subjected to solution treatment followed by aging at 490 °C for 2h. With regard to the tensile anisotropy, yield strength and ultimate tensile strength of the horizontally-built samples slightly exceeded those vertically-built. These findings are significant as they allow an informed prediction about the effect of various heat treatments on the microstructure and mechanical behaviour of components

manufactured from 18Ni-300 maraging steel using the SLM process.

Keywords: Selective laser melting; 18Ni-300 maraging steel; heat treatment; microstructure; mechanical behaviour

1 Introduction

In recent years, selective laser melting (SLM) has become one of the most promising additive manufacturing (AM) technologies worldwide due to its capability to directly manufacture complex-shaped metallic parts based on three-dimensional (3D) geometric models [1]. During the process, a high energy laser source selectively melts the metallic powder following a layered manner according to the 3D model of the part [2]. SLM is conceptually different from conventional manufacturing technologies, such as casting, forging, or machining [3]. Due to the rapid cooling and solidification rates (10^6-10^8 K/s) of the molten pool during SLM, which contributes to the formation of fine cellular microstructure, the as-built parts always exhibit better mechanical properties than those conventionally as-produced. Due to its prominent advantages, SLM has been employed in several high-value manufacturing sectors, including aerospace, automotive, and medical devices. A wide range of metallic powders have been successfully employed including titanium [4, 5], aluminium [6, 7], steels [8, 9], Ni-based alloys [10-12], metal matrix composites (MMCs) [13, 14], and some functional multi-materials [15, 16]. Due to the high levels of complexity and uncertainty during SLM, the performance of the final components depends on carefully selecting several important process parameters, including laser power, scanning speed, hatch spacing, layer thickness, and scanning strategy. Inadequate process parameters combinations lead to unacceptable defects, such as balling, cracks, pores, spatter, and residual stress [17-19].

18Ni-300 maraging steel is a class of low carbon iron-nickel alloys with high strength and toughness, good weldability and machinability. Several studies have successfully proven that this material is suitable for SLM, which have primarily focused

on either process parameters optimisation or mechanical properties after aging. For example, Casalino et al. [20] investigated the influence of process parameters on relative density in the SLM 18Ni-300 maraging steel through a successive statistical optimisation approach. The authors found that relative density of higher than 99% was produced using the laser power above 90 W and the scanning speed less than 220 mm/s. Bai et al. [19] conducted orthogonal experiments on process parameters optimisation of 18Ni-300 maraging steel. Their study found that high laser power or low scanning speed resulted in vaporisation and spatter. Kempen et al. [21] and Casati et al. [22] investigated the effect of various aging conditions on mechanical behaviours of SLM 18Ni-300 maraging steel and found that aging led to a significant increase in strength and a decrease in ductility compared with the as-built samples. Tan et al. [23], who also studied the effect of aging behaviour on the mechanical properties of 18Ni-300 maraging steel fabricated using SLM, found that one of the main hardening mechanism was ascribed to the precipitated-phase strengthening (Ni_3Ti, Ni_3Mo) after aging. Yin et al. [24] systematically investigated the effect of various aging temperatures (390-590°C) and time (1-7h) on the mechanical and tribological properties of SLM 18Ni-300 maraging steel. They found that the best performance was achieved after aging at 490°C for 3h. However, the authors did not consider the build directions of the samples.

Only a few number of studies have focused on the anisotropy of mechanical properties of SLM-fabricated 18Ni-300 maraging steel before and after heat treatments. Mutua et al. [25] investigated the tensile anisotropy of the as-built and solution-aging treated samples. They found that the vertically-built samples had lower tensile strength and elongation than those horizontally-built. Suryawanshi et al. [26] studied the tensile anisotropic behaviour of the samples that were subjected to aging at 480 °C for 5h. The authors found no tensile anisotropy, however, the anisotropy under other heat treatment conditions still remains unclear. Due to the significant temperature gradient in the molten pool during SLM, the formation of microstructure has strong anisotropic behaviour [27], which may lead to a difference in the mechanical performance of the samples fabricated during various build directions.

Accordingly, the objective of the present study is to further investigate the effect of heat treatment on microstructure and mechanical behaviour of 18Ni-300 maraging steel and explore the anisotropic behaviour at different build directions. The study employs X-ray diffraction (XRD), optical microscopy (OM) and scanning electron microscopy (SEM) to reveal the phase transformation and microstructure of the as-built and heat-treated samples. Furthermore, the tensile strength, fracture analysis, and microhardness are also investigated for as-built and heat-treated samples at different build directions to explore the mechanical performance and anisotropic behaviour.

2 Material and experimental methods

2.1 Powder characteristics

This study employed gas atomised 18Ni-300 maraging steel powder (Ni: 18.14, Co: 8.72, Mo: 4.88, Ti: 0.61, Al: 0.09, Cr: 0.42, Mn Si: 0.1, C: 0.02, and the balance Fe) supplied from Shining Technology (Chongqing Shining Technology Co., Ltd., China). The particle morphology of the powder was characterised by a scanning electron microscopy (FEI Nova 400 FEG-SEM). As shown in Fig. 1, the majority of the particles have a spherical shape and a number of large-sized particles have satellites attached to the surface. In addition, a small fraction of particles with irregular shapes were also observed.

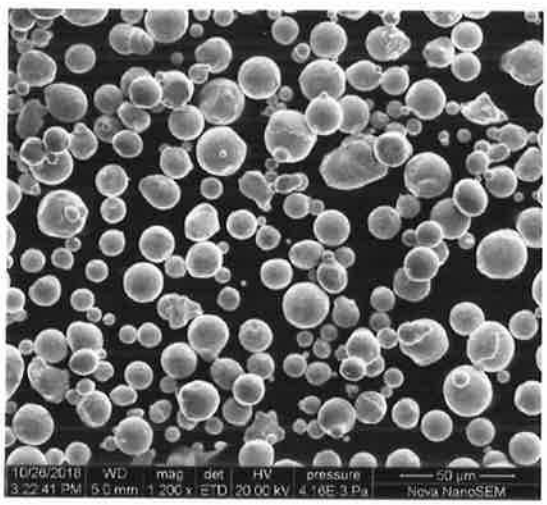

Fig. 1. SEM morphology of 18Ni-300 maraging steel powder.

2.2 SLM process

A metallic SLM machine (EP-M250, E-plus 3D Technology Ltd., China) equipped with a laser spot diameter of 70 μm, a maximum laser power of 500 W, and a maximum scanning speed of 2000 mm/s was employed to manufacture samples at room temperature. All the samples were fabricated on a 304 stainless steel substrate under the protection of nitrogen atmosphere.

Laser energy density is adopted to describe the relationship among laser power, scanning speed, hatch spacing, and layer thickness during the SLM; it is calculated as follows [28]:

$$E = \frac{P}{vhd} \tag{1}$$

where E, P, v, h, and d represent laser energy density (J/mm^3), laser power (W), scanning speed (mm/s), hatch spacing (mm), and layer thickness (mm), respectively.

In this study, to find the optimal process parameters, the laser energy density varied from 40 J/mm^3 to 80 J/mm^{3}and the laser power varied from 250 W to 350 W, while the hatch spacing and layer thickness were maintained at 120 μm and 30 μm, respectively. Herein, the laser scanning speed can be calculated according to Eq. (1). Table 1 shows the 25 process parameter sets. Fig. 2a shows the scanning strategy employed in this study. Every layer was divided into three zones to reduce the thermal stress, and the short reciprocating scanning line was adopted with a scanning rotational direction of 67° for the neighbouring layer. The zone overlap was maintained as 0.05 mm to guarantee fine metallurgy of every single track.

As shown in Fig. 2b, a set of cubic samples (10×10×10mm^3) were fabricated to investigate the influence of process parameter on surface morphology, relative density and metallurgical defects. After that, the optimum process parameters were employed to manufacture samples and study the microstructure and mechanical behaviour before and after various heat treatments. In addition, the samples were fabricated at horizontal and vertical directions to investigate the anisotropy of mechanical behaviours, which means that the horizontal direction was perpendicular to the applied loading direction, while the vertical direction was parallel to the loading direction.

Table 1 List of SLM process parameters.

Orders	Energy density (J/mm^3)	Laser power (W)	Scanning speed (mm/s)	Layer thickness (mm)	Hatch spacing (mm)
1	40	250	1302	0.03	0.12
2	40	275	1432	0.03	0.12
3	40	300	1563	0.03	0.12
4	40	325	1693	0.03	0.12
5	40	350	1823	0.03	0.12
6	50	250	1042	0.03	0.12
7	50	275	1146	0.03	0.12
8	50	300	1250	0.03	0.12
9	50	325	1354	0.03	0.12
10	50	350	1458	0.03	0.12
11	60	250	868	0.03	0.12
12	60	275	955	0.03	0.12
13	60	300	1042	0.03	0.12
14	60	325	1128	0.03	0.12
15	60	350	1215	0.03	0.12
16	70	250	744	0.03	0.12
17	70	275	818	0.03	0.12
18	70	300	893	0.03	0.12
19	70	325	967	0.03	0.12
20	70	350	1042	0.03	0.12
21	80	250	651	0.03	0.12
22	80	275	716	0.03	0.12
23	80	300	781	0.03	0.12
24	80	325	846	0.03	0.12
25	80	350	911	0.03	0.12

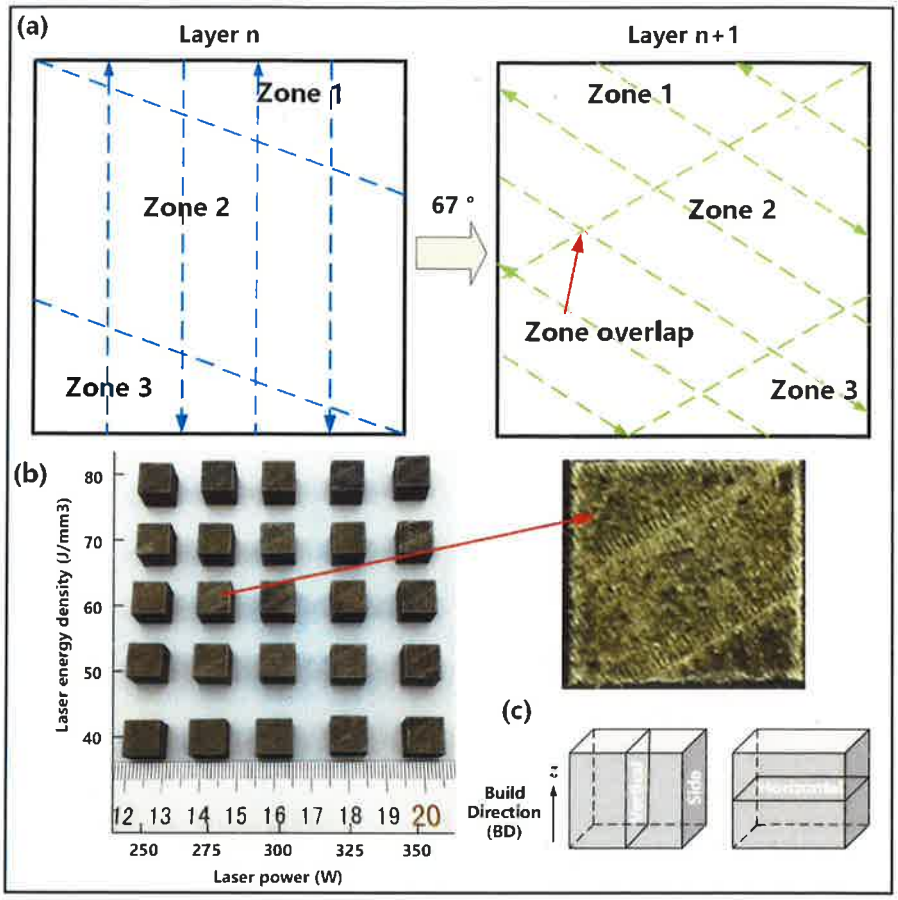

Fig. 2 Schematic diagram of (a) laser scanning strategy; (b) cubic samples used for process parameters optimisation; and (c) section strategy of the cubic sample.

2.3 Characterisation of process parameters optimisation

The top surface morphology of the as-built samples was observed by TESCAN VEGA3 LMH SEM. The samples were then sectioned (Fig. 2c) and polished prior to OM observation (Keyence VHX-1000 digital microscope) to study the relationship between process parameters and defects. An image analysis method (ImageJ) was used for the quantitative analysis of the relative density on the basis of the optical micrographs.

2.4 Post treatment

Horizontally built samples with cylinder shape were first machined in accordance with the size of the vertically built ones with a dog bone shape prior to heat treatments. To study the effect of heat treatment, some as-built samples were subjected to solution

treatment (ST) at 840°C for 2h, followed by water cooling and direct aging treatment (AT) at 490°C for 2h. Once the ST was completed, the STed samples were further aged at 200°C, 490°C and 650°C for 2h, 4h and 6h. Table 2 shows the heat treatment employed (conditions B – H); condition A provided the baseline for comparisons.

Table 2 Details of the heat treatment process investigated.

Condition	Heat treatment
A	No treatment, as-built via SLM
B	Solution treatment (ST) at 840 °C for 2h
C	Aging treatment (AT) at 490 °C for 2h
D	ST at 840 °C for 2h + AT at 490 °C for 6h
E	ST at 840 °C for 2h + AT at 200 °C for 4h
F	ST at 840 °C for 2h + AT at 490 °C for 2h
G	ST at 840 °C for 2h + AT at 200 °C for 6h
H	ST at 840 °C for 2h + AT at 650 °C for 6h

2.5 Microstructure analysis

For the microstructure analysis, the phase identification was performed by X-ray diffraction (XRD, D/MAX 2500PC, Japan) under Cu Kα radiation (150 mA, 40 kV) with a scanning step of 0.02° and a scanning speed of 4°/min. The microstructure in the vertical section was observed by OM and SEM. Prior to the characterisation, the polished sections were etched by a reagent consisting of 1 g $CuCl_2$, 25 ml HNO_3, 50 ml HCl, and 150 ml water.

2.6 Mechanical test and fracture characterisation

The Vickers hardness of the polished samples was measured by a hardness tester (MH-60, China) under a 500 g load for 8 s dwell time. Six different points of each sample were measured and averaged to determine the microhardness. The tensile tests were conducted at room temperature on the MTC landmark servohydraulic test system with a strain rate of 0.07 min^{-1}. Fig. 3 shows the tensile samples and tensile testing equipment used. Subsequently, a FEI Nova 400 SEM was used to observe the fracture morphology.

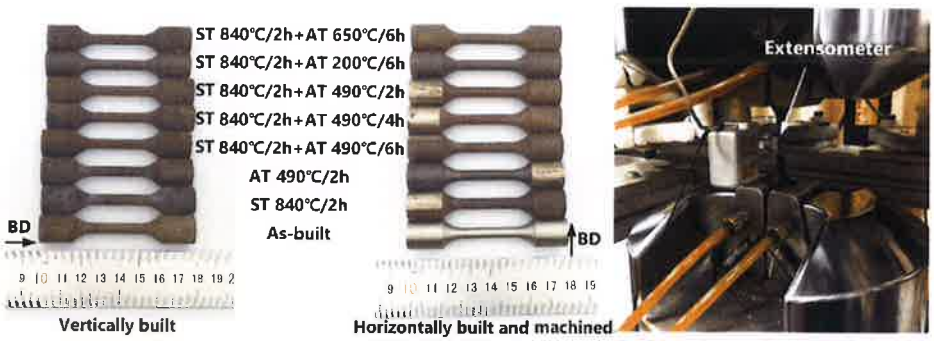

Fig. 3. Schematic diagram of the as-built and heat-treated tensile samples and tensile test set-up (ST indicates the solution treatment and AT indicates the aging treatment).

3. Results and discussion

3.1 Process parameters optimisation

3.1.1 Surface morphology

The top surface morphologies of the as-built cubic samples as related to laser energy density and laser power are shown in Fig. 4. When the laser power was fixed at 270 W, a poor surface finish was observed at lower laser energy density (E=40 J/mm^3). Discontinuous solidification tracks and a large number of balling with heterogeneous distributions were formed. Moreover, massive unmelted powder particles could be also observed (Fig. 4a). As the laser energy density increased to 60 J/mm^3, balling became less pronounced. However, discontinuous solidification tracks were still formed in some regions (Fig. 4b). It is known that the formation of balling at low laser energy density is ascribed to the significant temperature gradient and Marangoni convection effect within the molten pool [17]. With a further increase in laser energy density (E=70 J/mm^3), the surface presented the best state with a good surface finish and limited balling (Fig. 4c), revealing good metallurgies between neighbouring solidification tracks and layers.

However, with an increase in laser energy density to 80 J/mm^3, some defects (microcracks, soot particles and spatters) were observed, indicating that a continuous increase in laser energy density will not improve the surface finish (Fig. 4d). Due to the

increase in dwelling time of the laser beam resulted by higher laser energy density, more heat accumulation and higher temperature will be formed within the molten pool, which leads to the formation of microcracks during the cooling and solidification. Moreover, increasing laser energy density too much can lead to spatter, vaporisation and soot particles. When the laser density energy was 70 J/mm^3, some balling were obviously observed at both the laser power of 250 W and 300 W (Fig. 4e-f). Meanwhile, soot particles and spatters were formed at the laser power of 250 W, while discontinuous solidification tracks were formed at the laser power of 300 W. Additionally, the formation of the balling phenomenon was unavoidable during the SLM of 18Ni-300 maraging steel regardless of the applied laser energy density.

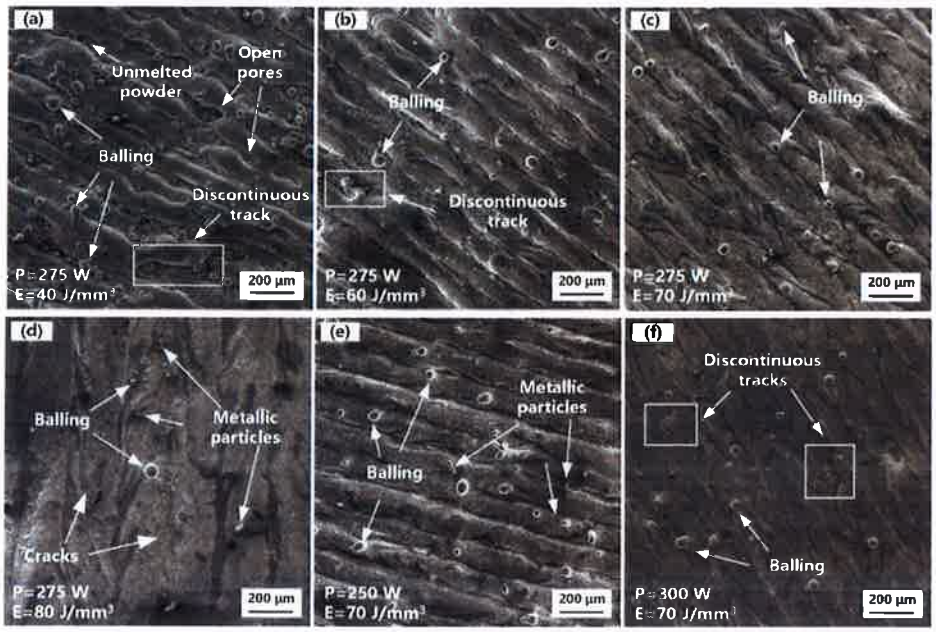

Fig. 4. SEM micrographs showing the top surfaces of the as-built samples with different process parameters.

3.1.2 Relative density

Fig. 5 shows that the fabrication of 18Ni-300 maraging steel parts with high relative density is significantly influenced by process parameters. The result indicated that higher laser energy density resulted in higher relative density when the laser power was

maintained constant. As shown, the lower relative density was achieved at the laser energy density of 40 J/mm^3, the sample with the lowest relative density of 89.72% was produced with laser power of 250 W. As a whole, the relative density increased with the increase in laser energy density. However, the relative density and laser energy density did not always offer a linear correlation. The relative density decreased slightly when the laser energy density and laser power were 80 J/mm^3 and 275 W, respectively, revealing that higher laser energy density leads to the reduction of the relative density. The sample exhibited a peak of relative density reaching up to 99.92%, when the laser energy density and laser power were fixed at 70 J/mm^3 and 275 W, respectively.

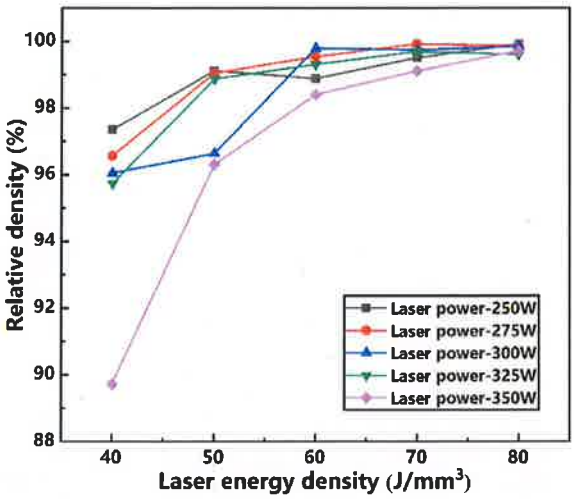

Fig. 5. The relative density of the as-built samples of 18Ni-300 maraging steel fabricated using different process parameters.

Fig. 6 shows the typical optical micrographs of the vertical (parallel to the build direction, BD) and horizontal (perpendicular to the BD) sections of the as-built cubic samples fabricated with various process parameters. Those inspections were useful for investigating the effect of process parameter on the relative density. When the laser power was fixed at 275 W, a large number of irregular pores were formed in both the vertical and horizontal sections at laser energy density of 50 J/mm^3(Fig. 6a-b). With an increase in laser energy density to 60 J/mm^3, a small number of observable pores were

formed in the vertical section, while a large number of irregular pores were still observed in the horizontal section. In particular, the irregular pores in the horizontal section were generally elongated along the laser scanning orientation. The formation of irregular pores at lower laser energy density is ascribed to the balling effect induced by insufficient fusion of the powder [18]. When the laser energy density increased to 70 J/mm^3, irregular pores completely disappeared and only a small number of spherical micropores were observed (Fig. 6e-f).

However, with an increase in laser energy density to 80 J/mm^3, a large number of spherical micropores appeared in both the vertical and horizontal sections (Fig. 6g-h). The size of micropores was larger than that at the laser energy density of 70 J/mm^3. Moreover, a small number of microcracks were also observed. Thus, the relative density slightly deceased. The microcracks formed at higher laser energy density are attributed to the residual thermal stress during SLM [17]. Microcracks could limit the mechanical properties of the as-built samples. Moreover, when the laser energy density was fixed at 70 J/mm^3, massive pores were formed in both the horizontal sections at the laser power of 250 W and 300 W (Fig. 6i-j). The above results were consistent with those of the surface morphology observation reported in Section 3.1.1.

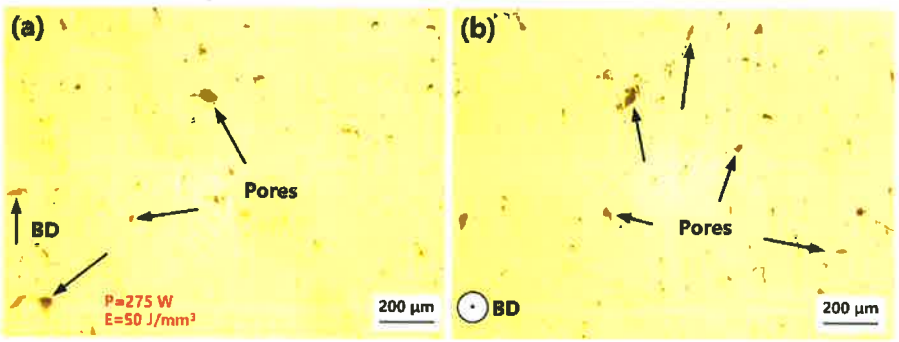

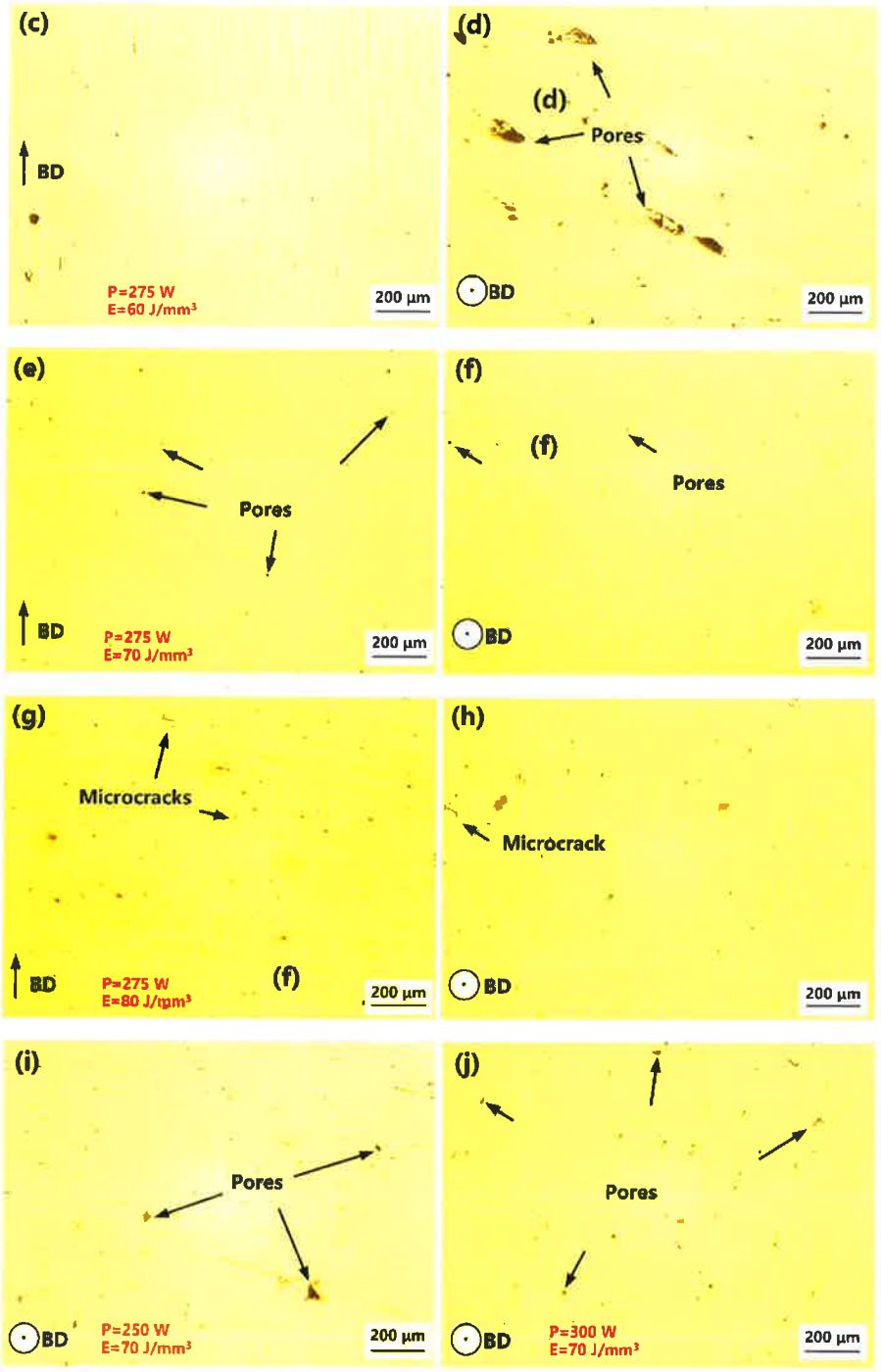

Fig. 6 Optical micrographs showing the vertical and horizontal sections of the as-built samples with different process parameters; BD indicates the build direction.

Fig. 7 depicts the corresponding optical micrograph of the polished/etched cross-sections of the sample with the highest relative density. As shown in Fig. 7a, semi-

elliptical shaped molten pool boundaries were visible with an approximate height of 33.5 μm. Meanwhile, elongated structures with an approximate width of 136 μm representing laser solidification tracks and rotation angle can also be observed in the horizontal section (Fig. 7b). Moreover, the solidification tracks between neighbouring scanning regions presented sufficient overlaps, indicating fine metallurgy for every single track.

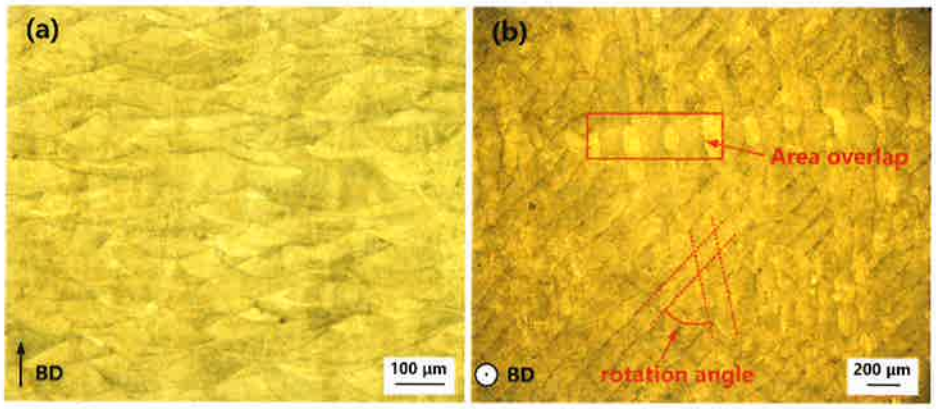

Fig. 7 Optical micrographs of the polished/etched sections of the samples with the laser energy density of 70 J/mm^3 and laser power of 275 W: (a) vertical view; (b) horizontal view; BD indicates the build direction.

As a result of the above analysis, the optimum laser energy density and laser power in the present work were determined to 70 J/mm^3 and 275 W, respectively, which contributed to nearly full densification of 18Ni-300 maraging steel with a smooth surface and fewer defects. The optimum process parameters were employed to manufacture samples for further investigations.

3.2 Phase and microstructure analysis

The XRD pattern of the as-built and heat-treated samples is presented in Fig. 8, which shows that the dominant microstructure consisted of martensite (α) phase for all conditions and the heat treatment resulted in phase transformation. A considerable number of martensite (α) phase was identified and austenite (γ) phase remained very low inside the as-built sample. After the sample was subjected to solution treatment at

840°C for 2h, no significant intensity peak of γ (200) was identified, indicating that the γ phase completely transformed into α phase. The intensity peak of γ (200) emerged again after aging treatment due to the occurrence of the reversion of α phase to γ phase during aging [29]. Moreover, no significant difference in the intensity peak of α (110) was identified between the as-built and direct aging treated samples.

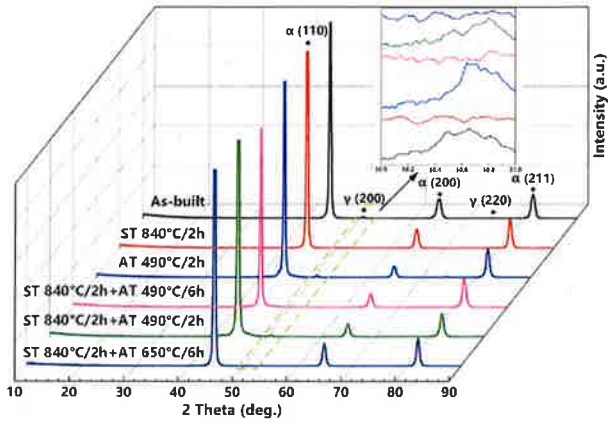

Fig. 8 XRD pattern of the as-built and heat-treated samples.

Fig. 9 presents three typical optical micrographs of the as-built and heat-treated samples. A large number of martensite phase was observed which was consistent with the XRD results. Fig. 10 shows the corresponding SEM micrographs of the samples. Fig. 10a-b illustrate the microstructure in the vertical section of the as-built sample. The SEM images showed that several cellular and columnar microstructures were observed in the vertical section, which was due to the difference in the cooling and solidification rates of the molten pool during SLM. Such similar behaviour of microstructure was also reported by Mutua et al. [25] and Han et al. [12]. The cellular microstructure had a size of several hundred submicrons, and the columnar microstructure was formed along the build orientation. Fine cellular and columnar microstructures can increase mechanical behaviours of the as-built samples. In comparison, Fig. 10 c-f show the microstructure of the heat-treated samples. It can be observed that the semi-elliptical shaped molten pool boundaries apparently disappeared (Fig. 10c and e). Moreover, cellular and columnar microstructures disappeared as the increase in grain size occurred

during the solution treatment, and a large number of lath martensite phase was observed, as shown in Fig. 10d and f.

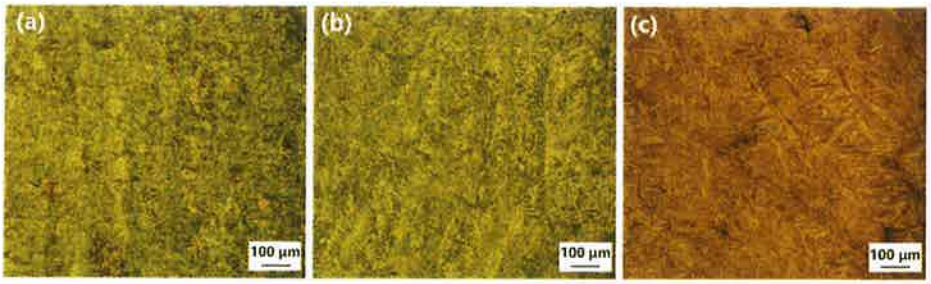

Fig. 9 OM micrographs on the vertical section of the samples: (a) as-built; (b) solution treated at 840°C for 2h; (c) solution treated at 840°C for 2h and aging at 490°C for 2h.

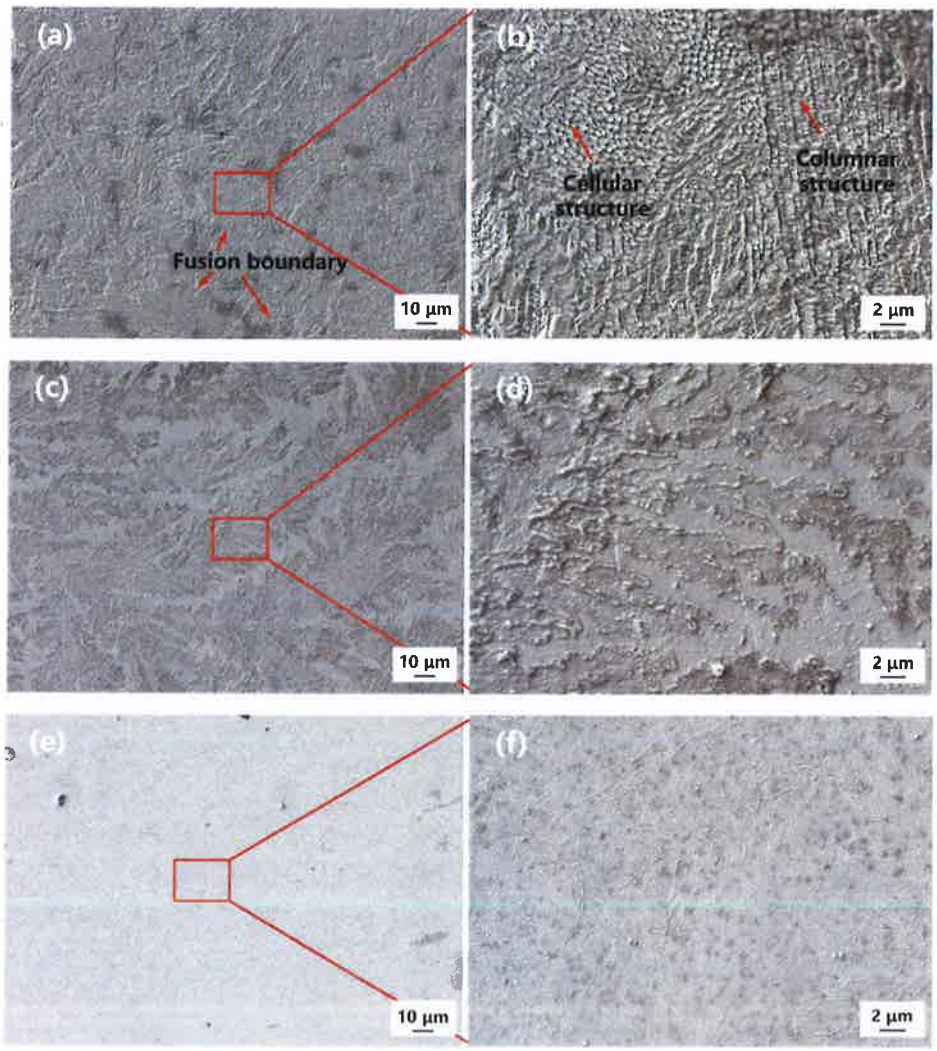

Fig. 10 SEM micrographs on the vertical section of the samples: (a, b) as-built; (c, d) solution treated at

840°C for 2h; and (e, f) solution treated at 840°C for 2h and aging at 490°C for 2h.

3.3 Mechanical properties analysis

3.3.1 Tensile behaviour and fracture analysis

The stress-strain curves of the as-built and heat-treated samples at different build directions are shown in Fig. 11. As shown in Fig. 11a, in the vertical direction, the as-built samples exhibited yield strength (YS) and ultimate tensile strength (UTS) of ~ 928 MPa and ~ 1016 MPa, respectively. The strength of the sample upon solution treatment at 840°C for 2h was obtained the lowest YS and UTS of ~ 609 MPa and ~ 903 MPa, respectively, indicating that solution treatment resulted in a decrease in strength. Several reasons may be attributed to this behaviour, including the increase in grain size, stress relief, and the elimination of microscopic segregation after solution treatment. However, there were obvious improvements in YS and UTS of the samples after aging treatments at 490 °C. The YS and UTS were improved to ~ 1775 MPa and ~ 1820 MPa, respectively, after direct aging at 490 °C for 2h. Compared to this heat treatment condition, the samples exhibited slightly lower YS and UTS (~ 1620 MPa and ~ 1691 MPa, respectively) after the solution treatment at 490 °C for 2h was followed by the same aging treatment. This improvement of strength is thought to be induced by the formation of the intermetallic precipitations (e.g., Ni_3Ti, Ni_3Mo, etc.) at the aging temperature of 490 °C, which can strengthen the martensitic matrix [21]. Additionally, the improvements in YS and UTS were not significant in terms of lower or higher aging temperatures (200 °C and 650 °C). This is because the lower or higher aging temperature leads to underaging or overaging results [24]. Both conditions played no significant role in the improvement of mechanical properties.

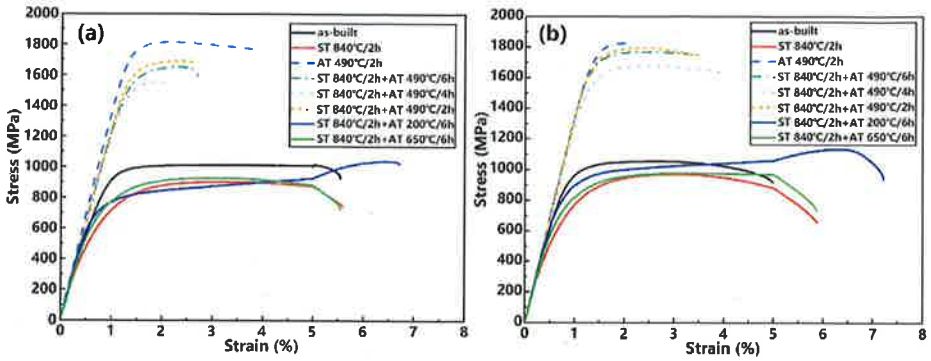

Fig. 11. Tensile stress-strain curves of the as-built and heat-treated samples at (a) vertical direction; (b) horizontal direction.

To compare the tensile anisotropic behaviours under different build directions, Fig. 12 summarises the YS and UTS of the as-built and heat-treated samples. It can be observed that the YS and UTS of the horizontally built samples slightly exceeded those vertically built. This is because of the formation of columnar grains along the build direction during SLM [11, 27]. However, the tensile anisotropic behaviour between vertical and horizontal build directions was not significant.

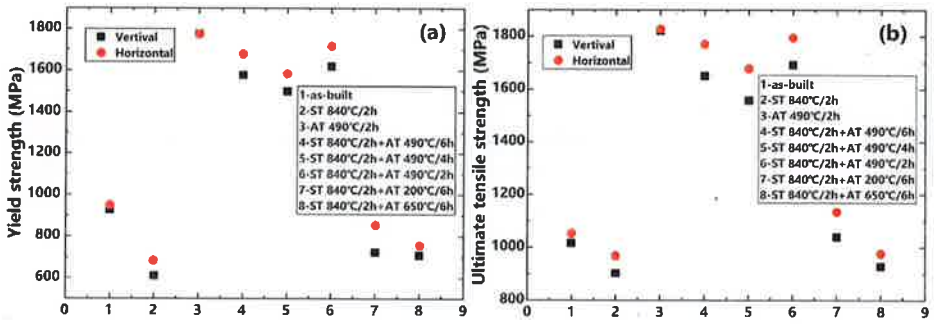

Fig. 12 Comparison of (a) YS and (b) UTS of the as-built and heat-treated samples with different build directions.

Fig. 13 shows three typical fracture surfaces of the as-built and heat-treated samples due to the similarity of the fracture features of the horizontally-built samples and the vertically-built ones. From a macroscopic perspective, several defects, including microcracks and pores, were formed in both the as-built and heat-treated samples, which may become the cracking source during stretching and also reduce the tensile

strength. At high magnification, a large number of dimples with a homogeneous size of ~ 1 μm in the fracture surface were observed in the as-built sample (Fig. 13a2-a3), suggesting a typical trans-granular ductile fracture of the as-built sample.

Fig. 13b shows the fracture morphology of the solution treated sample at 840 °C for 2h. It can be observed that there was an obvious plastic deformation feature in the fracture surface (Fig. 13b1). Moreover, a large number of deep dimples were observed at high magnification (Fig. 13b2-b3), indicating a similar fracture principle compared with that of the as-built samples. However, after aging, the fracture surface became flat and cleavage features were obvious (Fig. 13c1). Furthermore, dimple features were also observed as shown in Fig. 13c3. These two typical features revealed a mixed brittle and ductile fracture after aging treatment at 490°C for 2h.

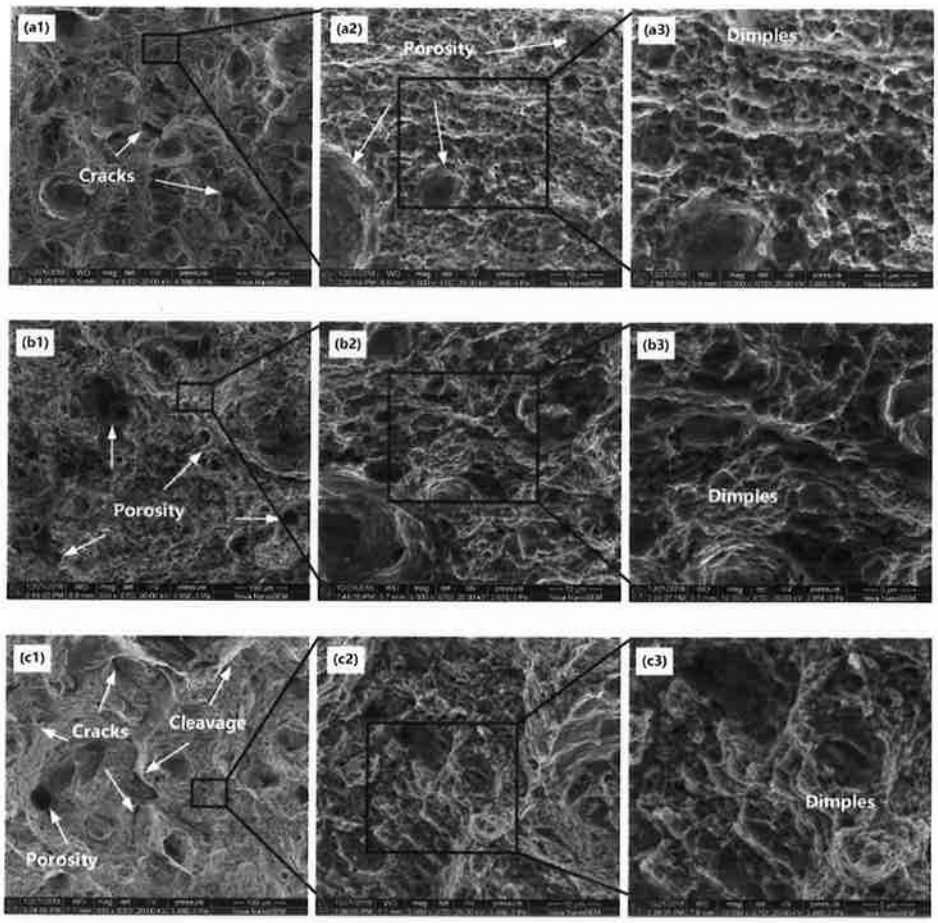

Fig. 13. Fracture morphologies of the samples: (a) as-built; (b) solution treated at 840°C for 2h; and (c)

solution treated at 840°C for 2h and aging at 490 °C for 2h.

3.3.2 Microhardness

The comparison of Vickers hardness measurements on the polished sections of the as-built and heat-treated samples (Fig. 14) shows no obvious anisotropic behaviour under the same condition of heat treatment. As illustrated, the microhardness of the as-built sample was 340 $HV_{0.5}$ on the side surface and 345 $HV_{0.5}$ on the top surface. However, the sample that was subjected to solution treatment at 840 °C for 2h achieved the lowest hardness of 294 $HV_{0.5}$ and 303 $HV_{0.5}$ on the side surface and top surface, respectively. As mentioned previously, the decrease in microhardness was attributed to grain growth and residual stress release during solution treatment. In addition, aging treatment played a notable role in the improvement of the hardness. The sample reached the peak hardness value of 543 $HV_{0.5}$ on the side surface and 532 $HV_{0.5}$ on the top surface upon solution treatment at 840 °C for 2h and aging at 490 °C for 2h. As mentioned, the occurrence of the increase in microhardness was due to the formation of intermetallic precipitations after aging treatment.

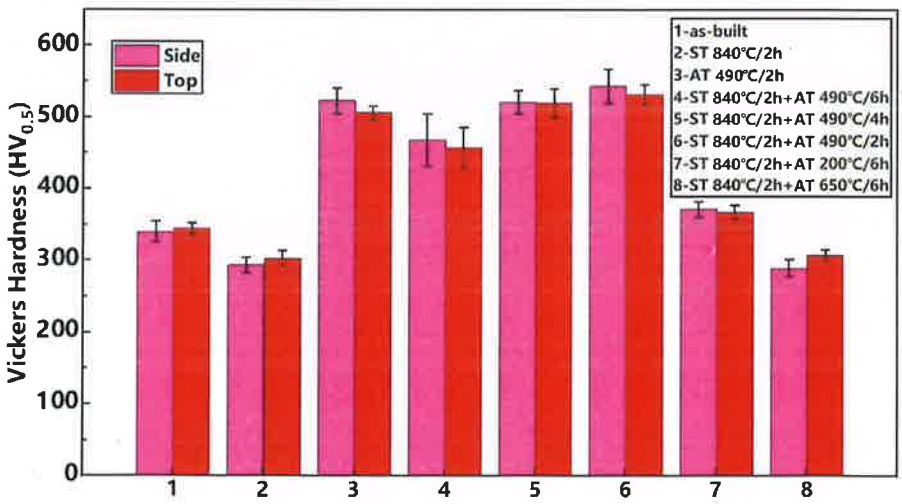

Fig. 14. Comparison of the Vickers hardness of the as-built and heat-treated samples.

3.4 Mold fabrication

Fig. 15a-b shows the application case of a mold with cooling channels manufactured using the SLM system and optimum process parameters discussed in Section 3.1. From a macroscopic perspective, the scanning strategy adopted in this study resulted in no obvious warp of the part that was induced by residual thermal stress during SLM. The top surface of the as-built mold was associated with a smooth surface and limited defects (Fig. 15d-e). However, the defects were detrimental to the surface roughness. Fig. 15c shows the surface roughness measurements of the as-built mold. The average roughness R_a on the top surface and side surface were measured to be 6.59 μm and 8.13 μm, respectively. The as-built part should be further processed by conventional methods for the requirement of high surface accuracy in the automotive domain. Moreover, the average microhardness on the top surface and side surface of the as-built component was 348.83 $HV_{0.5}$ and 344.18 $HV_{0.5}$ under a 500 g load for 8 s dwell time, respectively, while the microhardness increased to 577.80 $HV_{0.5}$ and 571.43 $HV_{0.5}$, respectively, after aging at 840 °C for 2h. The results were consistent with those discussed in Section 3.3.2. Therefore, the above findings could demonstrate the validity of the SLM process employed for mold manufacturing.

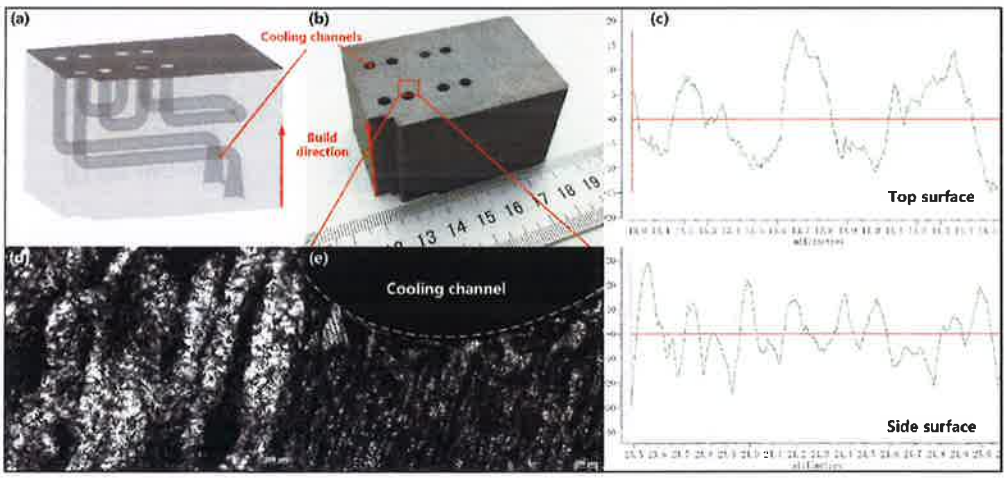

Fig. 15 SLM-manufactured mold with cooling channels: (a) CAD framework; (b) as-fabricated component; (c) surface roughness; and (d-e) top surface morphology.

4. Conclusions

In the present study, 18Ni-300 maraging steel parts were manufactured by SLM. The effect of heat treatment on microstructure and mechanical behaviour was investigated. Moreover, the tensile anisotropy and microhardness at different build directions were also studied. The important findings are summarised as follows:

(1). In terms of the quantitative analysis of the influence of process parameters including laser energy density and laser power on relative density, surface morphology and microstructure defects of the as-built samples, the optimum process parameters of 70 J/mm^3 energy density and 275 W laser power of 18Ni-300 maraging steel were obtained. The samples manufactured using the optimum process parameters exhibited the highest relative density of 99.92% among all samples with a smooth surface and fewer defects.

(2). Due to the different cooling and solidification rates in the molten pool during SLM, cellular and columnar microstructures were formed in the vertical section of the as-built samples. The solution treatment resulted in grain growth. As a result, the two kinds of microstructures disappeared and a large number of lath martensite was observed. Moreover, the XRD measurements showed that the main phase of the as-built sample was martensite phase. However, the austenite phase completely transformed into the martensite phase after the sample was subjected to solution treatment, while the austenite phase was formed again upon aging treatment because of the reversion from martensite to austenite.

(3). Heat treatment significantly influenced the mechanical behaviours of the SLM-built samples, including YS, UTS and Vickers hardness. After solution treatment at 840°C for 2h, YS, UTS and Vickers hardness decreased slightly. However, YS, UTS and Vickers hardness achieved peak values after the samples were subjected to aging at 490 °C for 2h. In addition, with regard to the anisotropy of the build directions, the tensile behaviour of the horizontally-built samples exhibited slightly higher than those vertically-built.

(4) The fabrication of a mold with cooling channels and the corresponding

experimental study demonstrated that the SLM process can be applied for mold manufacturing.

Acknowledgements

This work was supported by the National Key Research and Development Program of China (No. 2018YFB1701203); the National Natural Science Foundation of China, China (No. 51805052); Graduate Research and Innovation Foundation of Chongqing, China (No. CYB18024); the Fundamental Research Funds for the Central Universities (No. 2019CDCGJX221, 2018CDXYJX0019); and Chongqing Science and Technology Bureau (No. cstc2018 jszx-cyzdX0102).

References

[1] C. Qiu, C. Panwisawas, M. Ward, H.C. Basoalto, J.W. Brooks, M.M. Attallah, On the role of melt flow into the surface structure and porosity development during selective laser melting, Acta Mater. 96 (2015) 72-79.

[2] B. AlMangour, D. Grzesiak, T. Borkar, J. Yang, Densification behavior, microstructural evolution, and mechanical properties of TiC/316L stainless steel nanocomposites fabricated by selective laser melting, Mater. Des. 138 (2018) 119-128.

[3] L. Thijs, F. Verhaeghe, T. Craeghs, J.V. Humbeeck, J. Kruth, A study of the microstructural evolution during selective laser melting of Ti–6Al–4V, Acta Mater. 58 (2010) 3303-3312.

[4] Q. Feng, Q. Tang, Y. Liu, R. Setchi, S. Soe, S. Ma, L. Bai, Quasi-static analysis of mechanical properties of Ti6Al4V lattice structures manufactured using selective laser melting, Int. J. Adv. Manuf. Technol. 94 (2018) 2301-2313.

[5] Z. Wang, Z. Xiao, Y. Tse, C. Huang, W. Zhang, Optimization of processing parameters and establishment of a relationship between microstructure and mechanical properties of SLM titanium alloy, Opt. Laser Technol. 112 (2019) 159-167.

[6] Q. Han, H. Gu, S. Soe, R. Setchi, F. Lacan, J. Hill, Manufacturability of AlSi10Mg overhang structures fabricated by laser powder bed fusion, Mater. Des. 160 (2018) 1080-1095.

[7] T. Gu, B. Chen, C. Tan, J. Feng, Microstructure evolution and mechanical properties of laser Additive Manufacturing of high strength Al-Cu-Mg alloy, Opt. Laser Technol. 112 (2019) 140-150.

[8] Y. Liu, Z. Pang, J. Zhang, Comparative study on the influence of subsequent thermal cycling on microstructure and mechanical properties of selective laser melted 316L stainless steel, Appl. Phys. A 123 (2017).

[9] S. Ma, Q. Tang, Q. Feng, J. Song, X. Han, F. Guo, Mechanical behaviours and mass transport properties of bone-mimicking scaffolds consisted of gyroid structures manufactured using selective laser melting, J. Mech. Behav. Biomed. Mater. 93 (2019) 158-169.

[10] W. Tillmann, C. Schaak, J. Nellesen, M. Schaper, M.E. Aydinöz, K.P. Hoyer, Hot isostatic pressing

of IN718 components manufactured by selective laser melting, Addit. Manuf. 13 (2017) 93-102.

[11] D. Tomus, Y. Tian, P.A. Rometsch, M. Heilmaier, X. Wu, Influence of post heat treatments on anisotropy of mechanical behaviour and microstructure of Hastelloy-X parts produced by selective laser melting, Mater. Sci. Eng. A 667 (2016) 42-53.

[12] Q. Han, R. Mertens, M.L. Montero-Sistiaga, S. Yang, R. Setchi, K. Vanmeensel, B. Van Hooreweder, S.L. Evans, H. Fan, Laser powder bed fusion of Hastelloy X: Effects of hot isostatic pressing and the hot cracking mechanism, Mater. Sci. Eng. A 732 (2018) 228-239.

[13] Q. Han, R. Setchi, F. Lacan, D. Gu, S.L. Evans, Selective laser melting of advanced Al-Al2O3 nanocomposites: Simulation, microstructure and mechanical properties, Mater. Sci. Eng. A 698 (2017) 162-173.

[14] B. AlMangour, D. Grzesiak, J. Yang, Selective laser melting of TiB2/316L stainless steel composites: The roles of powder preparation and hot isostatic pressing post-treatment, Powder Technol. 309 (2017) 37-48.

[15] S.L. Sing, L.P. Lam, D.Q. Zhang, Z.H. Liu, C.K. Chua, Interfacial characterization of SLM parts in multi-material processing: Intermetallic phase formation between AlSi10Mg and C18400 copper alloy, Mater. Charact. 107 (2015) 220-227.

[16] J. Chen, Y. Yang, C. Song, M. Zhang, S. Wu, D. Wang, Interfacial microstructure and mechanical properties of 316L/CuSn10 multi-material bimetallic structure fabricated by selective laser melting, Mater. Sci. Eng. A 752 (2019) 75-85.

[17] D. Gu, Y. Hagedorn, W. Meiners, G. Meng, R.J.S. Batista, K. Wissenbach, R. Poprawe, Densification behavior, microstructure evolution, and wear performance of selective laser melting processed commercially pure titanium, Acta Mater. 60 (2012) 3849-3860.

[18] H. Attar, M. Calin, L.C. Zhang, S. Scudino, J. Eckert, Manufacture by selective laser melting and mechanical behavior of commercially pure titanium, Mater. Sci. Eng. A 593 (2014) 170-177.

[19] Y. Bai, Y. Yang, D. Wang, M. Zhang, Influence mechanism of parameters process and mechanical properties evolution mechanism of maraging steel 300 by selective laser melting, Mater. Sci. Eng. A 703 (2017) 116-123.

[20] G. Casalino, S.L. Campanelli, N. Contuzzi, A.D. Ludovico, Experimental investigation and statistical optimisation of the selective laser melting process of a maraging steel, Opt. Laser Technol. 65 (2015) 151-158.

[21] K. Kempen, E. Yasa, L. Thijs, J.P. Kruth, J. Van Humbeeck, Microstructure and mechanical properties of Selective Laser Melted 18Ni-300 steel, Phys. Procedia 12 (2011) 255-263.

[22] R. Casati, J. Lemke, A. Tuissi, M. Vedani, Aging Behaviour and Mechanical Performance of 18-Ni 300 Steel Processed by Selective Laser Melting, Metals 6 (9) (2016) 218.

[23] C. Tan, K. Zhou, W. Ma, P. Zhang, M. Liu, T. Kuang, Microstructural evolution, nanoprecipitation behavior and mechanical properties of selective laser melted high-performance grade 300 maraging steel, Mater. Des. 134 (2017) 23-34.

[24] S. Yin, C. Chen, X. Yan, X. Feng, R. Jenkins, P. O'Reilly, M. Liu, H. Li, R. Lupoi, The influence of aging temperature and aging time on the mechanical and tribological properties of selective laser melted maraging 18Ni-300 steel, Addit. Manuf. 22 (2018) 592-600.

[25] J. Mutua, S. Nakata, T. Onda, Z. Chen, Optimization of selective laser melting parameters and influence of post heat treatment on microstructure and mechanical properties of maraging steel, Mater. Des. 139 (2018) 486-497.

[26] J. Suryawanshi, K.G. Prashanth, U. Ramamurty, Tensile, fracture, and fatigue crack growth

properties of a 3D printed maraging steel through selective laser melting, J. Alloys Compd. 725 (2017) 355-364.

[27] M. Ni, C. Chen, X. Wang, P. Wang, R. Li, X. Zhang, K. Zhou, Anisotropic tensile behavior of in situ precipitation strengthened Inconel 718 fabricated by Addit. Manuf., Mater. Sci. Eng. A 701 (2017) 344-351.

[28] L. Thijs, F. Verhaeghe, T. Craeghs, J.V. Humbeeck, J. Kruth, A study of the microstructural evolution during selective laser melting of Ti – 6Al – 4V, Acta Mater. 58 (2010) 3303-3312.

[29] E.A. Jägle, P. Choi, J. Van Humbeeck, D. Raabe, Precipitation and austenite reversion behavior of a maraging steel produced by selective laser melting, J. Mater. Res. 29 (2014) 2072-2079.